Simulation of shear banding in heterophase co-deformation: Example of plane strain compressed Cu–Ag and Cu–Nb metal matrix composites

N. Jia [a,b,∗], F. Roters [b], P. Eisenlohr [b], D. Raabe [b,∗], X. Zhao [a]

[a] Key Laboratory for Anisotropy and Texture of Materials (MOE), Northeastern University, Shenyang 110819, China
[b] Max-Planck-Institut für Eisenforschung, D-40237 Düsseldorf, Germany

Abstract

The co-deformation and shear localization in heterophase alloys is studied using two-dimensional crystal plasticity finite element simulations on plane strain compressed Cu–Ag and Cu–Nb metal matrix composites. The aim is to study the fundamentals of micromechanics, co-deformation and shear banding in materials with heterophase interfaces. It is observed that, depending on the initial orientations of the crystals, co-deformation of the constituent heterophases often proceeds via collective mechanisms, i.e. by pronounced shear banding triggered by stress concentration at the interfaces. This phenomenon leads to highly localized strains within the bands, exceeding the average strain in part by two orders of magnitude. Shear band development is related to the inherent mechanical properties of each crystal and also to the properties of the abutting crystals. The predicted topology and nature of the cross-phase shear bands, i.e. the extreme local strains, significant bending of the interface regions, and sharp strain localization that propagates across the interfaces, agree well with experimental observations in cold-rolled composites. The simulations reveal that cross-phase shear banding leads to large and highly localized values of stress and strain at heterophase interfaces. Such information is essential for a better understanding of the micromechanical boundary conditions inside co-deformed composites and the associated shear-induced chemical mixing.

1. Introduction

In past decades, much attention was placed on understanding the development of shear bands. These are non-crystallographic band-like regions of concentrated plastic flow, which occur in practically all bulk metallic single- and polycrystalline materials subjected to plastic deformation [1–10]. When homogeneous and compatible dislocation or twinning deformation is hindered or associated with very high stress levels, shear banding sets in as a softening and localization mechanism that starts in individual grains and can proceed further across multiple interfaces without substantially altering its topological features [10,11]. The stacking fault energy (SFE) strongly influences the substructure evolution and strain hardening and, hence, the formation of shear bands [1,8,10–13]. If the preceding microstructure consists of elongated dislocation walls and cell blocks, such as those typically observed in metals with high or medium SFE, the shear bands are classified as copper-type [2,4,11]. If the microstructure consists of twin-matrix lamellae in low SFE materials, the shear bands are referred to as brass-type [1,3,12,13]. In either case, the microstructure that exists at the onset of shear banding hinders dislocation slip, as supported by experimental observations [11,14–17]. Specifically, when slip is confined to systems parallel to an existing microstructure, such as observed when band-like dislocation cells or twin-matrix lamellae prevail, formation of shear bands is promoted.

∗ Corresponding authors. Address: Key Laboratory for Anisotropy and Texture of Materials (MOE), Northeastern University, Shenyang 110819, China. Tel.: +49 6792340 (N. Jia).
E-mail addresses: jian@atm.neu.edu.cn (N. Jia), d.raabe@mpie.de (D. Raabe).

While shear banding in homophase metallic alloys has been studied in some detail in the past, little is known about such collective instability phenomena in heterophase metal matrix composites (MMC) with a microstructure constituting heterophase interfaces [18–22]. In two-phase metallic alloys, shear banding is particularly essential, since it not only governs the same phenomena as in homophase materials (large local strains and stresses), but it can also lead to intense chemical mixing of non-soluble adjacent phases and even to phase dissolution or phase transformation [18–20]. The shear band development in MMC is associated with two important microstructure phenomena. One is the effect of the difference in mechanical properties among the constituent phases on the initiation of shear bands. The other is the interface instability induced by large trans-interface shears associated with such bands. Experimental observations on a multilayered Al–0.3 wt.% Sc alloy produced by accumulative roll bonding (ARB) show that the relative hardening behavior of the adjacent Al and Al–Sc layers strongly influences shear band development [23]. As very high in-plane shear stress occurs at the interfaces between the phases, through-thickness shear banding initiates, and a marked curvature of layers occurs in the longitudinal section of the rolled sheet. This structure is also reported in many other heavily deformed binary or ternary systems, such as Cu–Au [24], Cu–Ag [25,26], Cu–Nb [22,27] and Cu–Ag–Nb [28,29]. This strain-induced interface instability is accompanied by a mechanical alloying process that is characterized by the mixing of elements within the shear banded regions and/or the solid-state amorphization, as revealed by atom probe tomography analysis and transmission electron microscopy [22,25,29]. Although the above-mentioned studies have profoundly improved knowledge about the deformation of composite materials, an understanding of the shear band formation in heterophase structures and its contribution to the mechanical alloying process is still lacking.

Therefore, shear banding in co-deformed MMC under plastic deformation by simulations is studied here. Owing to the excellent combination of strength and conductivity, as well as available literature data on MMC consisting of Cu or Ag as matrix and a face-centered cubic (fcc) metal or high melting body-centered cubic (bcc) metal as second phase [18–22,27,30], the model materials are Cu–Ag and Cu–Nb composites that are representative of fcc–fcc and fcc–bcc binary MMC, respectively. Plane strain compression of bicrystal samples is simulated using a two-dimensional crystal plasticity finite element (CPFE) framework that incorporates the non-crystallographic shear banding mechanism in addition to dislocation slip and mechanical twinning [31]. Both, crystallographic and non-crystallographic deformation mechanisms in MMC with heterophase microstructures are addressed. The simulation results are analyzed with respect to the inhomogeneity of the microstructures and plastic flow. It is found that, compared to single phase materials, more shear banding can be triggered in heterophase composites.

2. Simulation procedures

2.1. Constitutive formulations and material parameters

A CPFE model is used to simulate the mechanical behavior in Cu–Ag and Cu–Nb heterophase composites during plane strain compression. The model is based on a constitutive model that incorporates shear banding as a separate non-crystallographic deformation mechanism, in conjunction with dislocation slip and mechanical twinning [31,32]. The shear banding mechanism refers to the model developed by Anand et al. [33] for amorphous metals. The implementation of the different deformation mechanisms has been discussed in a recent work by Jia et al. [31]. The constitutive parameters for the Cu, Ag and Nb metallic phases are determined by fitting the macroscopic stress–strain curves obtained from uniaxial tensile tests of each pure metal [34–36], as listed in the Supplementary material. For the fcc Cu and Ag phases, 12 $\{111\}\langle110\rangle$ dislocation slip systems and 12 $\{111\}\langle112\rangle$ twinning systems are considered. For the bcc Nb phase, two types of slip systems with a common $\langle111\rangle$ direction, i.e. $\{110\}\langle111\rangle$ and $\{112\}\langle111\rangle$, are considered, but no bcc twinning is included.

2.2. Finite Element implementation

Based on the constitutive laws outlined in Ref. [31], the CPFE simulations are carried out using the MSC. Marc2010 finite element solver together with a user-defined material subroutine. The focus is on the simulation of fcc–fcc (Cu–Ag) and fcc–bcc (Cu–Nb) heterophase composites under plane strain compression. For the study of shear banding in materials with heterophase interfaces in micromechanical detail as a function of crystal orientation [31] and phase combination [27,37–41], the deformation of two types of heterophase bicrystals, i.e. fcc grain (Cu) plus fcc grain (Ag) and fcc grain (Cu) plus bcc grain (Nb), is simulated. Detailed results on shear band topology and governing micromechanisms are presented.

For all bicrystal simulations presented here, the modeled region is a portion of bulk material with thickness H_0 and length L_0 in undeformed state, as shown in Fig. 1. For simulating plane strain compression, the elongation direction (ED), normal direction (ND) and transverse direction (TD) are set to coincide with a Cartesian coordinate system, X, Y and Z, respectively. A prescribed displacement corresponding to the thickness reduction is applied to the top edge with a strain rate of $10^{-3}\,\mathrm{s}^{-1}$. The right edge is free to move in X direction. The left and bottom edges are constrained from moving in the X and Y directions, respectively. Multi-point constraints are applied to maintain the right edge straight during deformation. With the aim of understanding the influence of the initial orientations and phase combinations on shear banding, simulations with various types of initial bicrystal microstructures are performed.
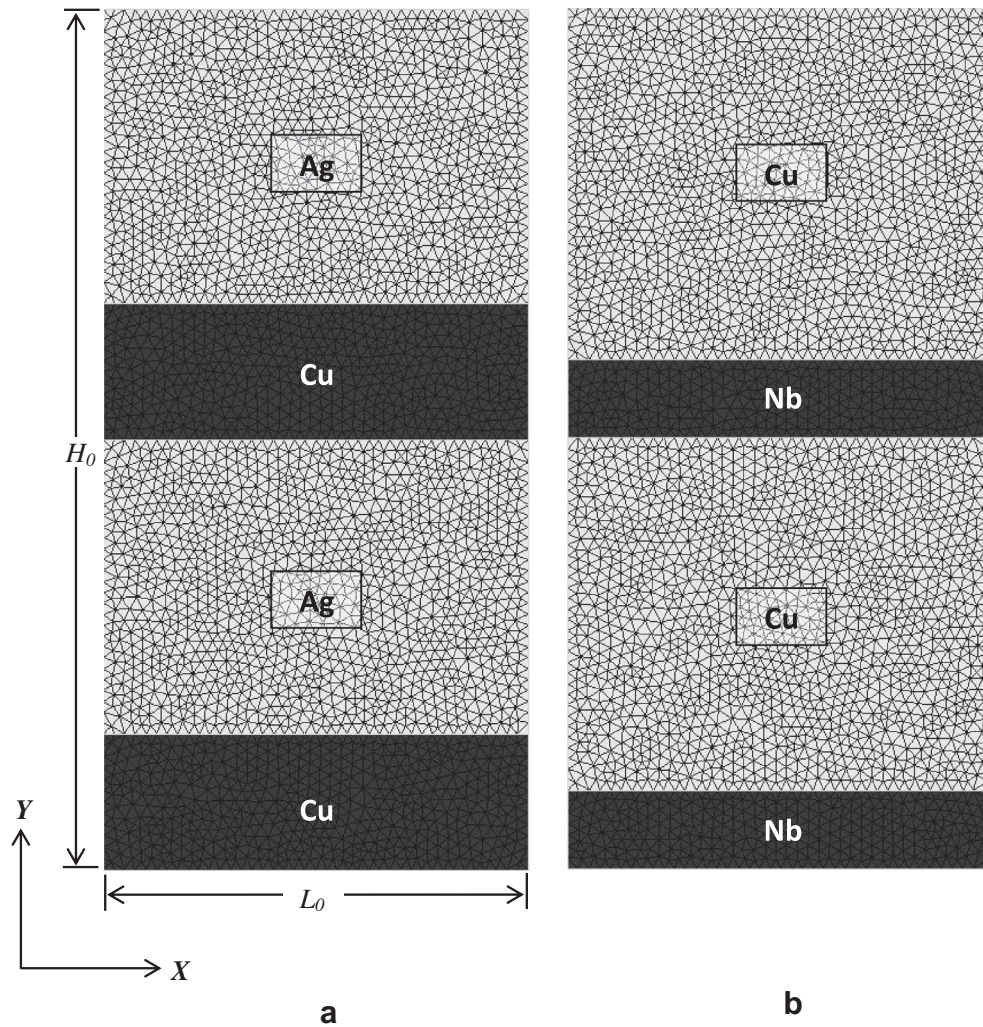
Fig. 1. Example of two-dimensional heterophase bicrystal finite element models consisting of triangular elements: (a) Cu–68.3 vol.% Ag (Cu phase in dark gray and Ag phase in light gray); (b) Cu–20 vol.% Nb (Cu phase in light gray and Nb phase in dark gray). To simulate plane strain compression, a prescribed displacement leading to thickness reduction is applied to the top edge. The left and bottom edges are constrained from moving in the X and Y directions, respectively. The right edge can freely move in X direction.

2.2.1. Heterophase composite consisting of two fcc grains

Fig. 1a shows the fcc plus fcc heterophase bicrystal model with a microstructure consisting of the mutually stacked Cu and Ag crystals. To mimic an initial eutectic composition of Cu–68.3 vol.% Ag [25], the thickness ratio between Cu and Ag crystals is 3:6.5. For the whole model, the thickness-to-length ratio is 0.5. The actual simulation runs are performed on three configurations with different initial orientation combinations (see Table 1): namely, Cu (copper orientation, $(112)[11\bar{1}])$ plus Ag $((112)[11\bar{1}])$; Cu $((112)[11\bar{1}])$ plus Ag (Goss orientation, $(011)[100])$; and Cu $((011)[100])$ plus Ag $((112)[11\bar{1}])$. In each model, the crystal is exactly oriented as an ideal component, i.e. all elements have the same initial orientation without any orientation scatter [42]. Finite element meshes with second-order isoparametric, six-noded, two-dimensional plane strain triangular elements are used. In each element, the same crystallographic orientation (of the crystal) is assigned to its three integration points.

Table 1
Miller indices and Euler angles of the ideal texture orientations in fcc and bcc metals.

Component	Indices $\{hkl\}\langle uvw \rangle$	Bunge (φ_1, Φ and φ_2)
Copper	$\{112\}\langle 111 \rangle$	90°, 35°, 45°
Goss	$\{011\}\langle 100 \rangle$	0°, 45°, 0°
Brass	$\{011\}\langle 211 \rangle$	35°, 45°, 0°
S	$\{123\}\langle 634 \rangle$	59°, 37°, 63°
Brass-R	$\{111\}\langle 112 \rangle$	90°, 55°, 45°
Rotated-cube	$\{001\}\langle 110 \rangle$	0°, 0°, 45°

2.2.2. Heterophase composite consisting of one fcc grain plus one bcc grain

The fcc plus bcc heterophase bicrystal model with a microstructure composed of the mutually stacked Cu and Nb crystals is shown in Fig. 1b. Different thicknesses are assigned to the different phases so that the overall composition is close to Cu–20 vol.% Nb [37]. The thickness-to-length ratio for the entire composite is 0.5. Simulations

on three configurations with different initial orientation combinations, i.e. Cu $((112)[11\bar{1}])$ plus Nb (Brass-R orientation, $(111)[11\bar{2}])$; Cu $((\bar{1}12)[11\bar{1}])$ plus Nb (Rotated-cube orientation, $(001)[1\bar{1}0])$; and Cu $((011)[100])$ plus Nb $((111)[11\bar{2}])$ are performed (see also Table 1). In addition, deformation of Cu, Ag and Nb single crystals with initial orientations that are advantageous for activating shear banding systems $((112)[11\bar{1}]$ for Cu and Ag, and $(111)[11\bar{2}]$ orientation for Nb) [31,43] is modeled. The same geometry and boundary conditions as those used for the bicrystals are applied also to the single crystal models.

3. Simulation results

3.1. Orientation-dependent shear banding for single crystals

An earlier study on single crystals with different initial crystallographic orientations in low SFE fcc metals [43] revealed that the tendency to initiate shear banding increases in fcc metals in the order: Goss, Cube, Brass-R and Copper-orientation. Therefore, in the current effort to study how shear bands develop in a heterophase microstructure with corresponding heterophase interfaces, the Copper $((112)[11\bar{1}])$ and Goss $((011)[100])$ orientations are selected as the initial components for both Cu and Ag. These are texture components promoting (Copper orientation) and preventing (Goss orientation) shear banding in fcc materials, respectively [31]. Considering the reciprocity of slip plane and slip directions for the 12 slip systems between fcc and bcc metals, i.e. $\{hkl\}_{\text{fcc}} = \langle uvw \rangle_{\text{bcc}}$ and $\langle uvw \rangle_{\text{fcc}} = \{hkl\}_{\text{bcc}}$ [37], we choose Brass-R $((111)[11\bar{2}])$ and Rotated-cube $((001)[1\bar{1}0])$ as initial orientations for the Nb phase [44]. These crystals represent the corresponding bcc crystal orientations facilitating (Brass-R) and preventing (Rotated-cube) shear banding in bcc materials, respectively.

The predicted equivalent true stress–equivalent true strain curves of the Ag, Cu and Nb single crystals with different initial orientations are shown in Fig. 2. In the second row of the same figure, the relative shear contributions of the competing deformation systems (dislocation slip, twinning, shear banding) as a function of the equivalent true strain are shown. The individual contributions are given as summations over the absolute values of the shear rates on the different systems for each type of mechanism, and then normalized by the overall shear amount at each time step. The deformation stage corresponding to a shear contribution of 0.1 from shear banding is marked by "○". For the Ag and Cu crystals with initial $(112)[11\bar{1}]$ orientation and the Nb crystal with initial $(111)[11\bar{2}]$ orientation, the model predicts that 0.1 shear band contribution occurs at a stress of 0.16, 0.28 and 0.32 GPa, respectively. This reveals that, when the stress reaches those values for the respective
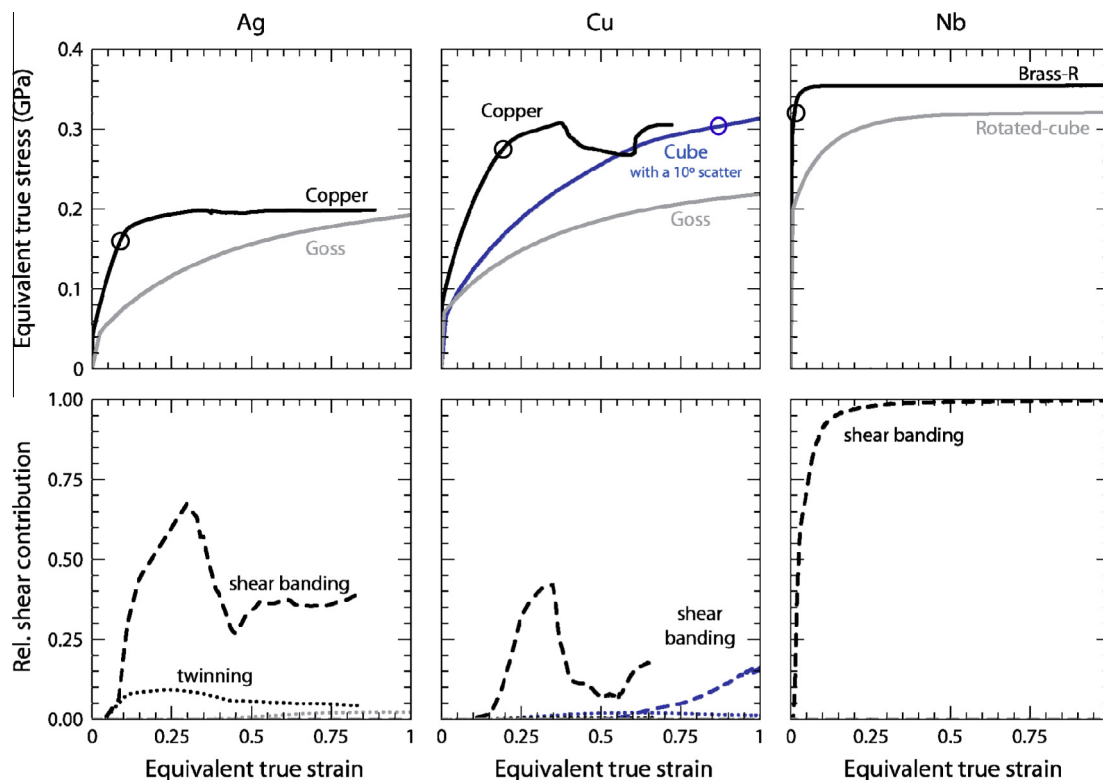

Fig. 2. Predicted stress–strain curves and relative shear contributed by the different deformation mechanisms (twinning and non-crystallographic shear banding) as a function of the equivalent true strain for bulk Ag, Cu and Nb single crystals with different initial crystallographic orientations $((112)[11\bar{1}]$ (Copper), $(011)[100]$ (Goss), $(001)[100]$ (Cube), $(111)[11\bar{2}]$ (Brass-R), and $(001)[1\bar{1}0]$ (Rotated-cube)) during plane strain compression. As the total shear contribution from dislocation slip, twinning and shear banding for each textured material is 1.0, the relative shear from dislocation slip is not shown.

metals, shear banding starts to be a significant deformation mechanism. For the Copper-textured Ag, an early activation of shear banding is predicted at a strain of 0.07. An increase in the twinning shear contribution is also found at this stage, and the maximum appears at 0.25 strain. With further deformation, the three mechanisms compete against each other. The initially Goss-oriented Ag crystal shows shear via dislocation slip on a constant high level and zero shear contribution of shear banding during plastic straining. The predictions for the Ag single crystals generally agree with a previous study on the orientation-dependent shear banding behavior of α-brass [31,43]. Compared with the simulations for Ag crystals with different initial orientations, the simulations for Cu crystals show similar shear contributions of dislocations and shear bands. For the initially Brass-R textured Nb single crystal, the simulation predicts that the decrease in shear contribution from dislocations together with the increase in the shear contributed by shear banding occur at a very early stage of deformation. In addition, further deformation proceeds mainly via shear banding rather than via dislocation slip. These data show that, in this material, the shear band systems are readily activated. For the initially Rotated-cube textured Nb material, shear banding does not occur over the entire deformation range.

3.2. Mechanical response of heterophase bicrystals

3.2.1. Heterophase composite consisting of two fcc grains

To explore the micromechanisms in the Cu–Ag composite subjected to plane strain compression, the simulated results for the bicrystals with various orientation combinations are presented in terms of the distribution of equivalent logarithmic strain, sum of shear rates on the shear band systems, and equivalent Cauchy stress at different thickness reductions, as shown in Fig. 3. It is emphasized that the present finite element analyses represent two-dimensional deformations. This means that the macroscopic shear band inclination along the transverse direction cannot be predicted in the present framework [45]. The principal stresses that matter for the constitutive shear band law are derived by principal axis transformation from the second Piola–Kirchoff stress tensor.[1] These principal stresses are ordered according to $|\sigma_1| \geqslant |\sigma_2| \geqslant |\sigma_3|$ with $\sigma_1 \leqslant 0$, $\sigma_2 \leqslant 0$, $\sigma_3 \geqslant 0$. For plane strain compression, the shear stress in the plane constructed by the two orthonormal principal directions $\hat{\mathbf{e}}_1$ and $\hat{\mathbf{e}}_3$ (corresponding to the maximum compression stress and the tensile stress) promotes mainly shear banding. Then, in the shear banding region, one would only expect two shear band systems activated on the $(\hat{\mathbf{e}}_1 - \hat{\mathbf{e}}_3)$ plane. For the sake of brevity, the simulation results for the Cu, Ag and Nb single crystals

---

[1] The non-crystallographic shear band systems are defined relative to the three principal directions of the second Piola–Kirchoff stress $\mathbf{T}^e$ [31]. The decomposition of $\mathbf{T}^e$ is: $T^e = \sum_{i=1}^{3} \sigma_i \hat{\mathbf{e}}_i \otimes \hat{\mathbf{e}}_i$, where σ_i are the principal stresses, and $\hat{\mathbf{e}}_i$ the orthonormal principal directions of $\mathbf{T}^e$.

are included in the Supplementary material, which provides a direct comparison with their bicrystal counterparts.

For the Cu $((1\,1\,2)[1\,1\,\bar{1}])$ plus Ag $((1\,1\,2)[1\,1\,\bar{1}])$ bicrystal (Fig. 3a), at 20% deformation the strain pattern in the Ag phase is similar to that in single-phase Ag (Fig. S2, Supplementary material), except for the sharper localization with a width below five elements in the former aggregate. In the Cu phase, strain is localized in the area connected to the localization of the Ag phase. The initiation of the shear band systems, which does not necessarily correspond to the occurrence of localized strain alone, is identified in both phases. It is observed that shear bands in the upper Cu crystal are triggered by stress concentration at the phase boundaries, since shear banding appears first in the bottom Ag crystal. With increasing deformation, shear banding in the Cu crystal is also activated. At higher deformations, shear bands appear to cross the phase boundaries and extend into the upper Ag crystal. At this stage, phase boundaries are generally straight, although some inclination with respect to ED at small angles as well as some minor curvature can be identified. In the interior of the crystals, different directions of strain localization appear in order to accommodate the plastic deformation at the phase boundaries. Moreover, the stress in the Cu phase is larger than that in the Ag phase. In the respective phases, the area with larger stress coincides with the material points where shear banding initiates. When the thickness reduction reaches 40%, very significant bending of the regions near the phase boundaries is predicted, and zones of sharp strain localization penetrate through the curved heterophase boundaries. At this stage, strain localization is pronounced in both phases, with a maximum variation in the local strain (true strain) among the constituent material points of ~3.5. The curved phase boundaries correspond to the material points where shear band regions intersect the interfaces. In the upper Cu crystal and in both Ag crystals, two families of shear bands are identified. The initiation of the second shear band is associated with stress concentration at the phase boundaries close to the left bounding edge of the model. The highly compacted mesh elements are related to strain localization, indicating that the elements in those areas have been severely distorted.

Fig. 3b shows the simulation results for the Cu $((1\,1\,2)[1\,1\,\bar{1}])$ plus Ag $((0\,1\,1)[1\,0\,0])$ bicrystal. Compared with the corresponding phases in the Cu $((1\,1\,2)[1\,1\,\bar{1}])$ plus Ag $((1\,1\,2)[1\,1\,\bar{1}])$ bicrystal, at 20% deformation, strain localization becomes weaker in the Ag phase, but remains at the same level in the Cu phase. Since the Cu phase has an initial orientation that promotes shear banding, the strain localized regions in the different phases are connected with each other at those material regions of the Cu crystals where significant shear banding appears. This observation shows that the local constraints that are exerted from a phase with shear bands reaching an interface promote localization also in its neighbor phase. At 33% thickness reduction, very severe shear banding accompanied by significant strain localization appears in the Cu phase. Strain

localization also occurs in the lower Ag crystal between the left and right edges. However, no shear banding is activated in this phase with its initial (0 1 1)[1 0 0] orientation.

Fig. 3c shows the results for the Cu ((0 1 1)[1 0 0]) plus Ag ((1 1 2)[1 1 1̄]) bicrystal. In this sample, the Ag phase is

mechanically stronger than the Cu phase. At 20% deformation, the strain localized region has an angle of ∼40° with respect to the ED. This pattern is close to that of the Copper-oriented Cu and Ag single crystals (Figs. S1 and S2, Supplementary material). However, shear banding is only
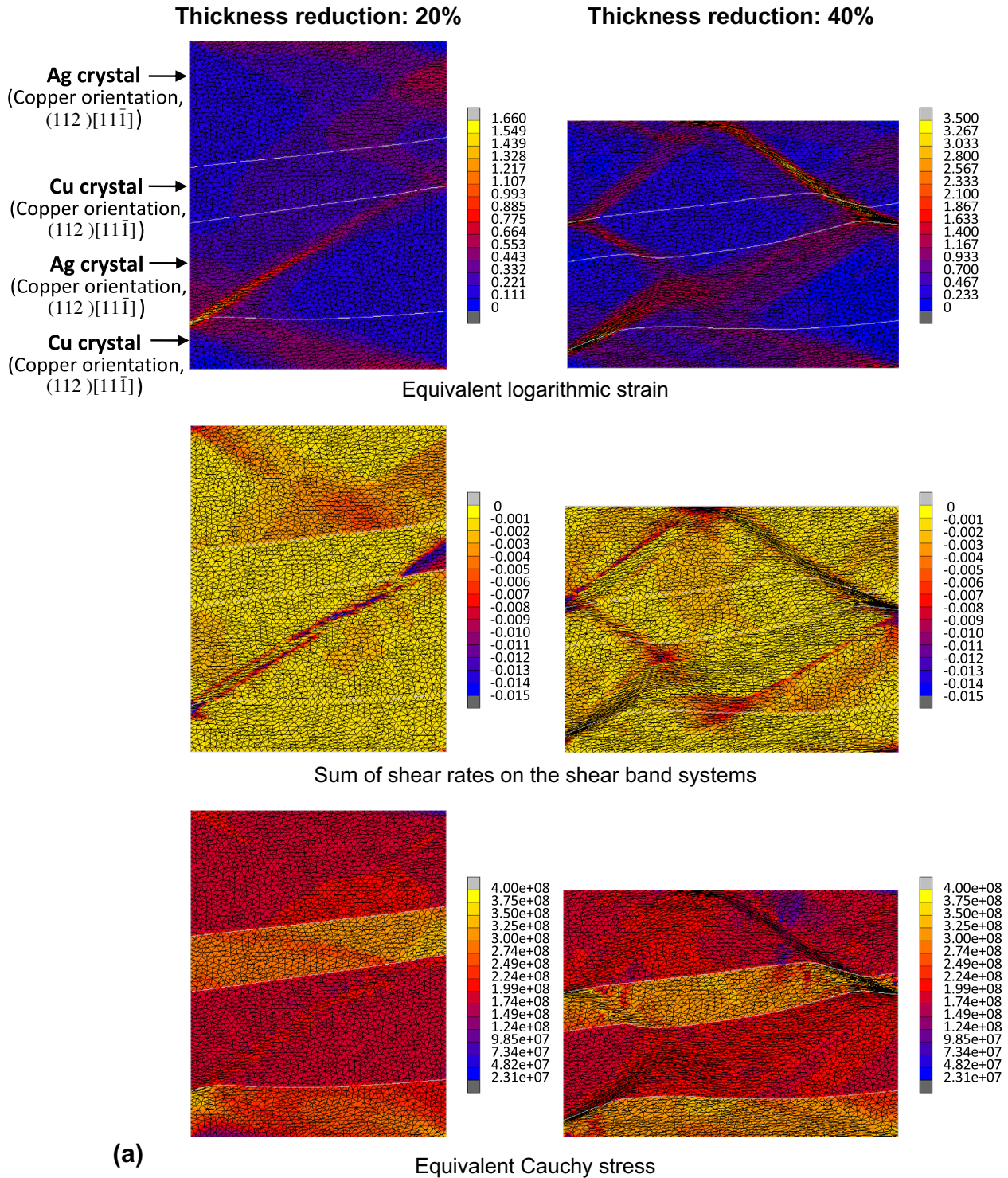

(a)

Fig. 3. Predicted distributions of equivalent logarithmic strain, sum of shear rates on the shear band systems and equivalent Cauchy stress for bicrystals with different initial orientations at 20% and higher thickness reductions: (a) Cu (Copper orientation, (1 1 2)[1 1 1]) plus Ag (Copper orientation, (1 1 2)[1 1 1]) heterophase bicrystal; (b) Cu (Copper orientation, (1 1 2)[1 1 1]) plus Ag (Goss orientation, (0 1 1)[1 0 0]) heterophase bicrystal; (c) Cu (Goss orientation, (0 1 1)[1 0 0]) plus Ag (Copper orientation, (1 1 2)[1 1 1]) heterophase bicrystal. In these models, white lines indicate interfaces between abutting crystals.
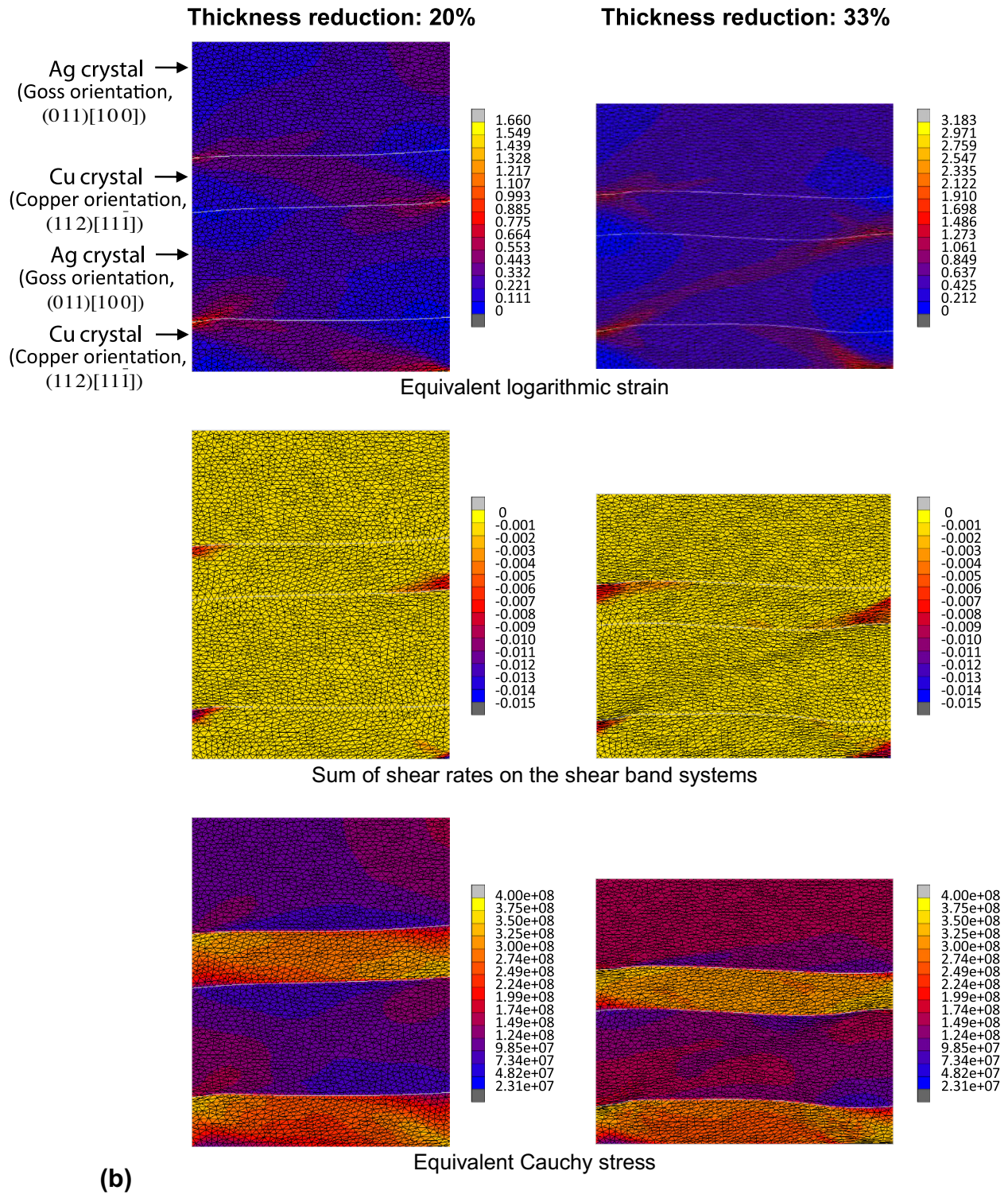
(b)

Fig. 3. (*continued*)

activated in the Ag phase. At 40% deformation, pronounced strain localization (with the maximum variation of the local true strain among the constituent material points of ∼3.5) is predicted. Phase boundaries of the upper Cu crystal have been largely rotated to be approximately aligned with the strain-localized region, with very severe distortion of the elements inside that zone. With the same color coding as that used for the case of 20% deformation, the shear rate of the shear band contours shows a weaker variation throughout the sample at higher deformations. In the Ag phase, shear banding is identified at the border of the strain localized zone, suggesting that, at high defor-
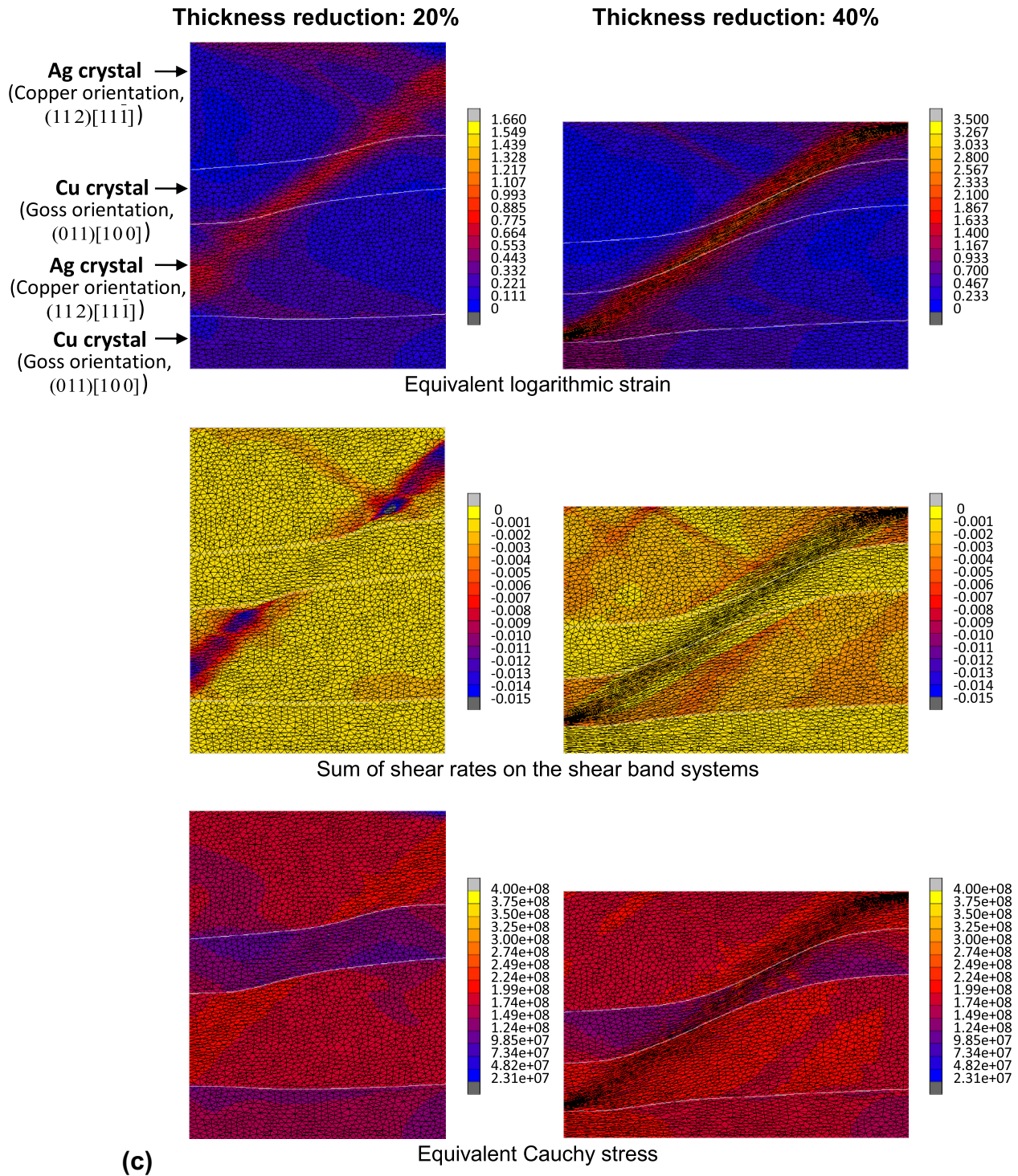
Thickness reduction: 20%   **Thickness reduction: 40%**

Equivalent logarithmic strain

Sum of shear rates on the shear band systems

Equivalent Cauchy stress

(c)

Fig. 3.   (*continued*)

mations, shear banding plays a major role in accommodating the imposed deformation between shear bands and regions outside these bands.

3.2.2. Heterophase composite consisting of one fcc grain plus one bcc grain

The simulation results for the Cu–Nb bicrystals with various orientation combinations under plane strain compression are presented in Fig. 4. For the Cu ($(1\,1\,2)[1\,1\,\bar{1}]$)

plus Nb ($(1\,1\,1)[1\,1\,\bar{2}]$) bicrystal (Fig. 4a), weak shear banding is identified at 20% deformation in the Cu phase between the left and right bounding edges of the sample. This behavior is similar to that in single-phase Cu. A significant localization of both strain and shear banding appears inside the Cu and Nb crystals. The localized zones are connected across the heterointerfaces, indicating that the initiation of shear banding in Cu (adjacent to Nb crystals) is triggered by stress concentration at the phase boundaries.

At 33% deformation, a more significant true strain accumulation (~5.0) occurs in both phases, indicative of the increasing incompatibility of deformation between the Cu and Nb phases. This leads to severe curvature of the phase boundaries connecting to the localized zones, which also agrees with experimental observations of such cold-rolled

Thickness reduction: 20% **Thickness reduction: 33%**

Cu crystal → (Copper orientation, $(112)[11\bar{1}]$)

Nb crystal → (Brass-R orientation, $(111)[11\bar{2}]$)

Cu crystal → (Copper orientation, $(112)[11\bar{1}]$)

Nb crystal → (Brass-R orientation, $(111)[11\bar{2}]$)

Equivalent logarithmic strain

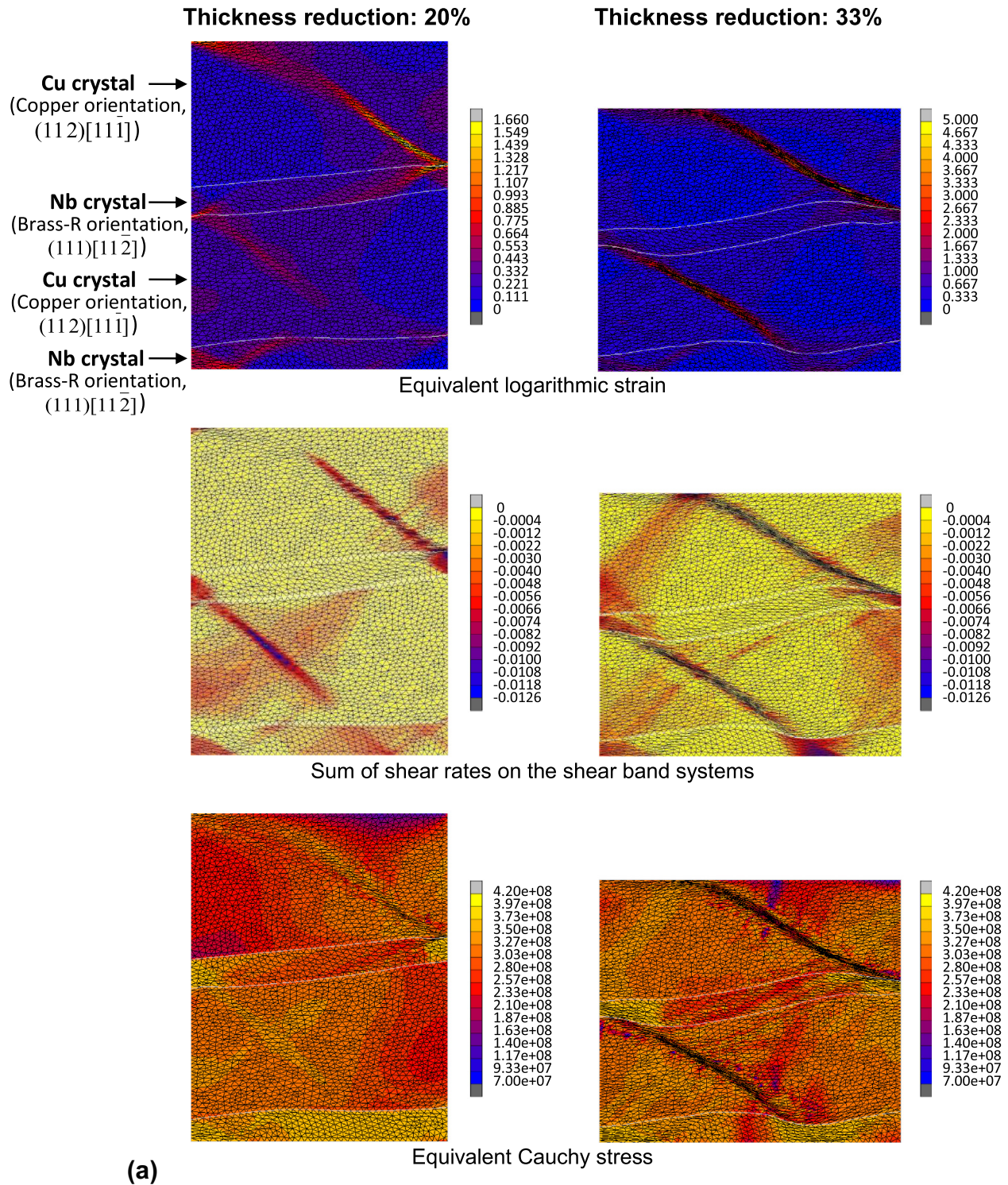Sum of shear rates on the shear band systems

Equivalent Cauchy stress

(a)

Fig. 4. Predicted distributions of equivalent logarithmic strain, sum of shear rates on the shear band systems and equivalent Cauchy stress for bicrystals with different initial orientations at 20% and higher thickness reductions: (a) Cu (Copper orientation, $(112)[11\bar{1}]$) plus Nb (Brass-R orientation, $(111)[11\bar{2}]$) heterophase bicrystal; (b) Cu (Copper orientation, $(112)[11\bar{1}]$) plus Nb (Rotated-cube orientation, $(001)[1\bar{1}0]$) heterophase bicrystal; (c) Cu (Goss orientation, $(011)[100]$) plus Nb (Brass-R orientation, $(111)[11\bar{2}]$) heterophase bicrystal. In these models, white lines indicate interfaces between abutting crystals.
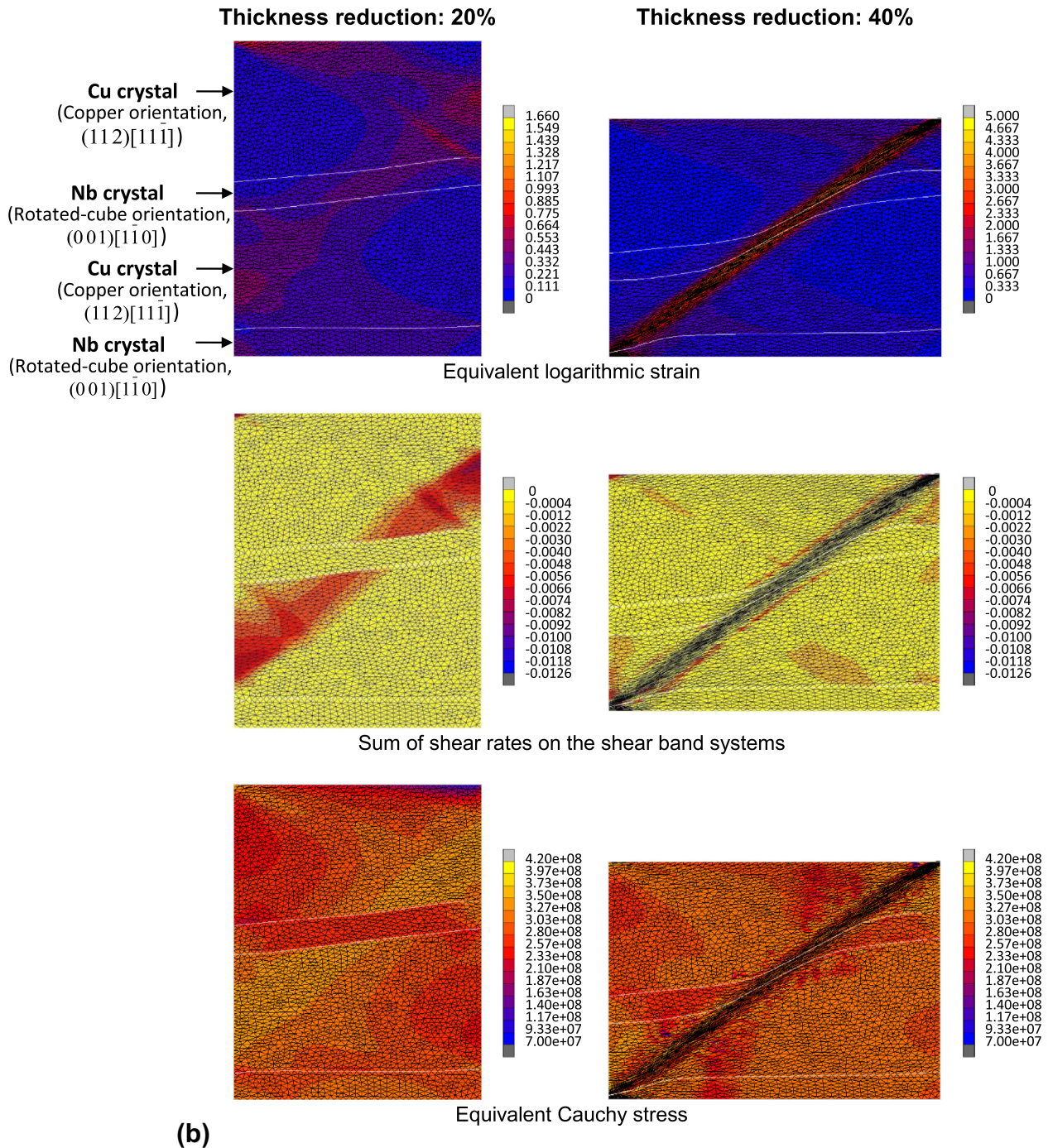
(b)

Fig. 4. (*continued*)

composites [22,24–29]. Moreover, it is revealed that at higher deformation, more shear bands that penetrate the Cu and Nb crystals are activated close to the top and bottom edges as well as to the left and right bounding edges of the sample. This shear banding pattern is consistent with the stress distribution. As both phases have initial orientations that promote shear banding, the activation of the shear bands can be triggered in either phase, provided that the local stress in this phase reaches the respective critical value to initiate shear banding. In this configuration, the

Nb phase is harder than the Cu phase. Therefore, the inhomogeneous strain distribution in the Cu phase tends to form at the material points near the Nb phase where the mechanical contrast is the highest. A similar result is also predicted in the softer phase (Ag) of the Cu $((1\,1\,2)[1\,1\,\bar{1}])$ plus Ag $((1\,1\,2)[1\,1\,\bar{1}])$ bicrystal sample (Fig. 3a). This picture agrees with the observation in an ARB processed Cu–Zr sheet, where the varying grain morphology in the Cu phase is attributed to an inhomogeneous deformation near the harder Zr phase [25].
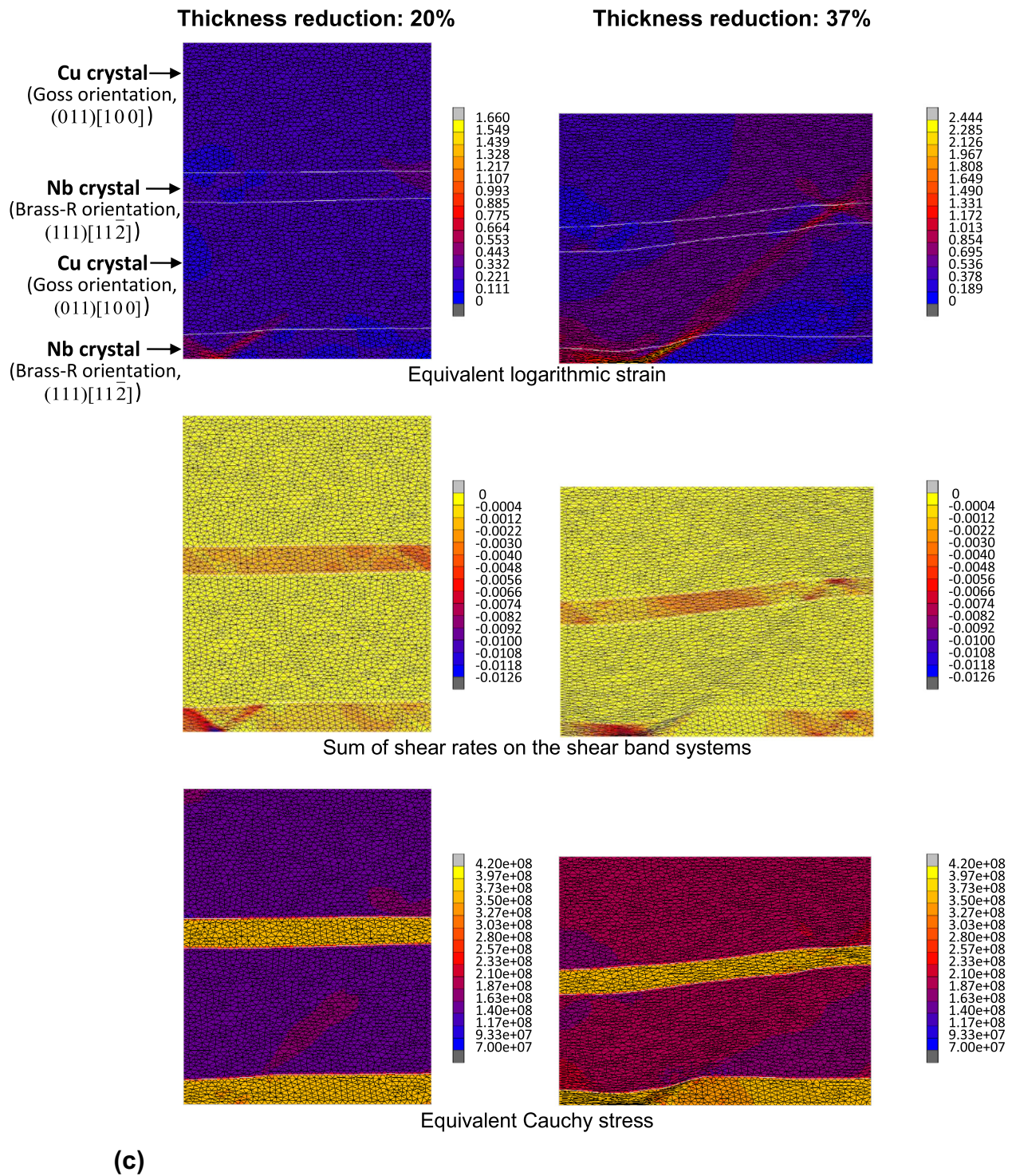
Thickness reduction: 20% **Thickness reduction: 37%**

Cu crystal →
(Goss orientation,
$(0\,1\,1)[1\,0\,0]$)

Nb crystal →
(Brass-R orientation,
$(1\,1\,1)[1\,1\,\bar{2}]$)

Cu crystal →
(Goss orientation,
$(0\,1\,1)[1\,0\,0]$)

Nb crystal →
(Brass-R orientation,
$(1\,1\,1)[1\,1\,\bar{2}]$)

Equivalent logarithmic strain

Sum of shear rates on the shear band systems

Equivalent Cauchy stress

(c)

Fig. 4. (*continued*)

For the Cu ($(1\,1\,2)[1\,1\,\bar{1}]$) plus Nb ($(0\,0\,1)[1\,\bar{1}\,0]$) bicrystal, the simulated patterns of strain, shear rate of the shear band systems, and stress are similar to that of the Cu ($(0\,1\,1)[1\,0\,0]$) plus Ag ($(1\,1\,2)[1\,1\,\bar{1}]$) sample (Fig. 3c). These results indicate that—triggered by stress concentration at the phase boundaries—the localized strain can readily propagate through the minority phase, even though it has

an orientation that is not susceptible to shear banding [31,43]. As shown in Fig. 4b, at 20% deformation strain, localization inclined to the ED by about 40° appears between the left and right bounding edges of the sample. The pattern is also similar to that of the Cu single crystal with an initial Copper orientation ($(1\,1\,2)[1\,1\,\bar{1}]$), although shear banding is only identified in the Cu phase, but not

in the Nb phase. Moreover, the stress is comparable in the different phases, except for some accumulation in the shear banding region of the Cu phase. This is consistent with the stress–strain curves of the single-phase samples (Fig. 2). At 40% deformation, larger shear rates associated with shear banding are predicted only in the Cu phase, although a strong strain localization that crosses phase boundaries (with the maximum variation of local true strain of ∼5.0) occurs in both phases.

Fig. 4c shows the simulation results for the Cu ($(0\,1\,1)[1\,0\,0]$) plus Nb ($(1\,1\,1)[1\,1\,\bar{2}]$) bicrystal. Compared with the Cu ($(1\,1\,2)[1\,1\,\bar{1}]$) plus Nb ($(1\,1\,1)[1\,1\,\bar{2}]$) bicrystal at 20% deformation, strain localization in the Cu phase is less significant. In addition, the localized strain in the Nb phase also becomes weaker, owing to the accommodation of the stress at the heterointerfaces. Since the Nb phase has an initial orientation that promotes shear banding, the strain localized regions in the different phases are connected to each other at the material points of the Nb crystals where the shear band systems are initiated. At 37% thickness reduction, very severe shear banding accompanied by significant true strain localization (∼2.4) is seen in the Nb phase. It is interesting to see that in the lower Cu crystal strain localization appears between the top and bottom phase boundaries, leading to severe bending of the interface regions. This means that the localized strain could also propagate through the matrix phase Cu, although in this phase no intrinsic shear banding is activated because of its initial orientation. It is also noted that at ∼40% deformation, for samples composed of only one phase susceptible to shear band formation, e.g. Cu ($(1\,1\,2)[1\,1\,\bar{1}]$) plus Ag ($(0\,1\,1)[1\,0\,0]$) and Cu ($(0\,1\,1)[1\,0\,0]$) plus Nb ($(1\,1\,1)[1\,1\,\bar{2}]$) samples, the color coding of strain contours is with relatively low maximum magnitude compared with other bicrystals. This is due to the fact that in these cases, the matrix phase (the Ag phase in Cu–Ag and the Cu phase in Cu–Nb) is much softer than its abutting phase, which leads to more homogeneous deformation of the overall samples.

4. Discussion

4.1. Shear banding behavior in bicrystals with different orientation/phase combinations

As demonstrated above, the initiation of shear banding depends on the initial orientation of crystals and their inherent mechanical properties [31,43]. According to the current simulations for the bicrystals with various initial orientation and phase combinations, the shear banding behavior of each individual crystal is found to be also influenced by the phase and orientation of the abutting crystals, in addition to the inherent properties of the crystal. The evolution of the normalized shear rates on the twinning and shear band systems for those crystals that are susceptible to shear band formation owing to their specific initial orientations, i.e. the Copper-oriented Cu and Ag crystals

and the Brass-R-oriented Nb crystal, is presented in Fig. 5. The results indicate the varying shear banding behavior of the same crystal embedded in different surrounding microstructures. Moreover, for selected thickness reductions, the interphase stress, i.e. the phase-to-phase interaction calculated from the difference in equivalent Cauchy stress between each considered phase and its abut-
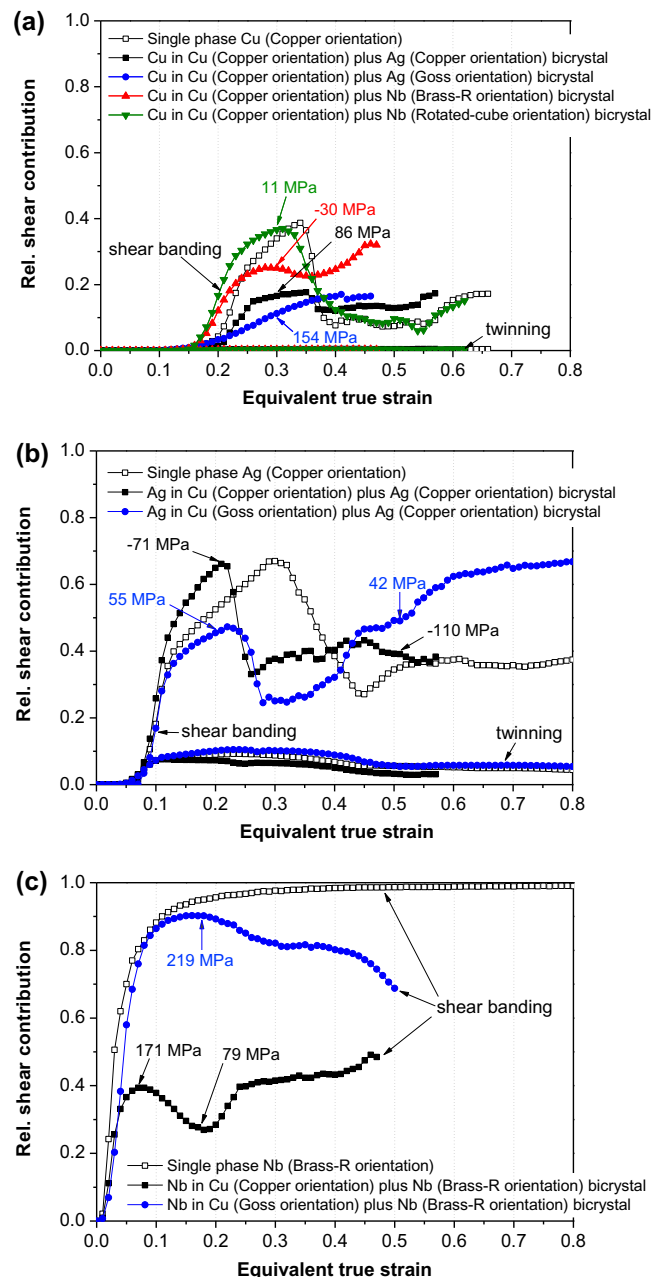

Fig. 5. Predicted relative shear contributed by the different deformation systems (twinning and non-crystallographic shear banding) as a function of the equivalent true strain for (a) Copper-oriented Cu crystal, (b) Copper-oriented Ag crystal and (c) Brass-R-oriented Nb crystal. The interphase stress calculated from the difference in equivalent Cauchy stress between each considered phase and its abutting phase for selected thickness reductions, i.e. the σ^{Cu}–$\sigma^{Ag\ or\ Nb}$, σ^{Ag}–σ^{Cu} and σ^{Nb}–σ^{Cu} values, are indicated in figures (a)–(c), respectively.

ting phase (the σ^{Cu}–$\sigma^{Ag\ or\ Nb}$, σ^{Ag}–σ^{Cu} and σ^{Nb}–σ^{Cu} values), is indicated in the figure.

For the Cu crystals (Fig. 5a), all simulations show a pronounced contribution of shear bands to the overall deformation at ∼25% thickness reduction (0.3 strain). However, the magnitude of their respective contribution to the deformation is different among the different bicrystals, i.e. the contribution from shear bands increases in the order: Cu ((112)[11$\bar{1}$]) plus Ag ((011)[100]) bicrystal, Cu ((112)[11$\bar{1}$]) plus Ag ((112)[11$\bar{1}$]) bicrystal, Cu ((112)[11$\bar{1}$]) plus Nb ((111)[11$\bar{2}$]) bicrystal, Cu ((112)[11$\bar{1}$]) plus Nb ((001)[1$\bar{1}$0]) bicrystal. This result is consistent with the stress discontinuity near the phase boundary in each sample. More specifically, in the Cu phase the shear banding contribution is more significant as the abutting phase becomes mechanically stronger. For the Cu ((112)[11$\bar{1}$]) plus Ag ((011)[100]) bicrystal, the Cu phase is stronger than the Ag phase during the whole period of deformation. As the strain has to be accommodated between the abutting phases, load redistribution occurs inside the sample. This leads to a mild increase in the stress in the hard phase and to rapid stress increase in the soft phase as a function of loading. Hence, the shear band activity in the Cu phase is reduced with the coexistence of the Ag phase. As seen in Fig. 3b, in Cu crystals shear banding is only identified in regions close to both phase boundaries and to the left and right bounding edges of the model. In contrast, for the co-deformed Cu ((112)[11$\bar{1}$]) plus Nb ((111)[11$\bar{2}$]) bicrystal, the Cu phase behaves as soft phase, and the Nb phase is relatively hard. Then in the Cu phase of this sample, more shear banding is activated than for the Cu ((112)[11$\bar{1}$]) plus Ag ((011)[100]) bicrystal (Fig. 4a). The Cu ((112)[11$\bar{1}$]) plus Nb ((001)[1$\bar{1}$0]) bicrystal displays a minor interphase stress, indicating that the mechanical properties of the phases are close to each other. Thus, the shear banding behavior of the Cu phase in the bicrystal is similar to that of single-phase Cu, which is determined mainly by the boundary conditions applied to the model (Fig. 4b). Accordingly, simulations for this sample and single phase Cu show a quite similar contribution of shear banding to the overall deformation (Fig. 5a). For the Ag crystals (Fig. 5b), at the initial stage of deformation the pronounced contribution of shear bands appears at ∼20% deformation (0.21 true nominal strain). A higher contribution from shear bands to the overall deformation is found in the Cu ((112)[11$\bar{1}$]) plus Ag ((112)[11$\bar{1}$]) bicrystal, which is consistent with the findings for Cu single crystals. More specifically, when the Ag phase coexists with a stronger phase, more shear banding is triggered at the boundaries between the phases (Fig. 3a). In the Cu ((011)[100]) plus Ag ((112)[11$\bar{1}$]) bicrystal, shear bands are induced by the boundary conditions of the model, rather than the incompatible stress at phase boundaries (Fig. 3c). When the thickness reduction reaches ∼40% (0.51 true strain), a rapid increase in the shear band contribution occurs in the Cu ((011)[100]) plus Ag ((112)[11$\bar{1}$]) bicrystal, as a

result of the strain-hardening of the Ag phase at this stage. However, the Cu ((112)[11$\bar{1}$]) plus Ag ((112)[11$\bar{1}$]) bicrystal shows a weaker contribution from shear bands compared with the specimen deformed to ∼20% strain. This is attributed to the fact that shear banding activated at the early stage of deformation induces a significant stress relaxation in the Ag phase. Thus, at large deformations, only minor shear banding is activated in Ag crystals, although the Cu phase continues to be stronger. For the Nb crystals (Fig. 5c), simulations show pronounced shear banding at an early deformation stage, i.e. at ∼7% thickness reduction (0.07 true strain) in the Cu ((112)[11$\bar{1}$]) plus Nb ((111)[11$\bar{2}$]) bicrystal and at 18% reduction (0.18 true strain) in the Cu ((011)[100]) plus Nb ((111)[11$\bar{2}$]) bicrystal, respectively. In addition, less contribution from shear bands is found in both samples compared with single-phase Nb, which agrees with the analysis above, namely, that less shear banding occurs when the abutting phase is mechanically soft. Furthermore, compared with the Cu ((112)[11$\bar{1}$]) plus Nb ((111)[11$\bar{2}$]) bicrystal more intense shear banding is predicted in the Cu ((011)[100]) plus Nb ((111)[11$\bar{2}$]) bicrystal. This is because in the latter case, the softer Cu phase constitutes a larger volume fraction of the sample and hence accommodates more plastic deformation than the Nb phase. This means that in the Cu ((011)[100]) plus Nb ((111)[11$\bar{2}$]) bicrystal the Cu crystals deform more homogeneously compared with the Nb crystals (Fig. 4c). Accordingly, the large stress in the Nb phase contributes to the significant activation of shear banding.

4.2. Micromechanics and co-deformation in heterophase MMC

To this stage, the assumption that specific microstructures, i.e. microbands or lamellar microstructures, are a necessary precursor to shear band formation as suggested by other works [14,15,46] is supported by the current predictions. Beyond that, it is observed that the activation of the shear band systems is related not only to the crystallographic orientations of the constituent grains, but also to the topology and constitutive properties of the heterophase microstructures within a sample. In order to observe such shear banding behavior when modified by different types of microstructures even more clearly, a simulation of a Cu (Cube orientation) plus Ag ((112)[11$\bar{1}$]) bicrystal is performed. In this sample, the Cu crystal is not susceptible to shear band formation compared with the Cu crystal originally oriented with the (112)[11$\bar{1}$] orientation, but shows potential for shear banding when a high enough stress is reached within the crystal. The initial texture scatter of the Cu phase is described in the form of a spherical Gauss component [47,48] with a full width at half maximum of 10°, while the other model parameters are the same as those used for Cu–Ag samples presented above. It should be pointed out that, by performing finite element modeling on an ideally Cube-oriented Cu single crystal under plane strain load, only a uniform dislocation-related

microstructure evolves (not shown here). This result is not consistent with the experimental observation that micro-shear bands have formed within deformation bands in a cold-rolled Cube single crystal of Cu at ~40% thickness reduction [49]. The discrepancy is attributed to the fact that the deformation banding is associated with local shears along the TD, while the current simulation can represent deformation only in the ED–ND plane due to the use of the two-dimensional elements. However, for single crystals with an initial texture scatter about the Ideal Cube component, both, the current simulation on single-phase Cu as well as the previous numerical study on α-brass [43] show that shear banding occurs at ~50% thickness reduction, and contributes to the overall deformation at a comparable level as dislocation slip when ~80% reduction is reached. The stress–strain curve and relative shear contributed by
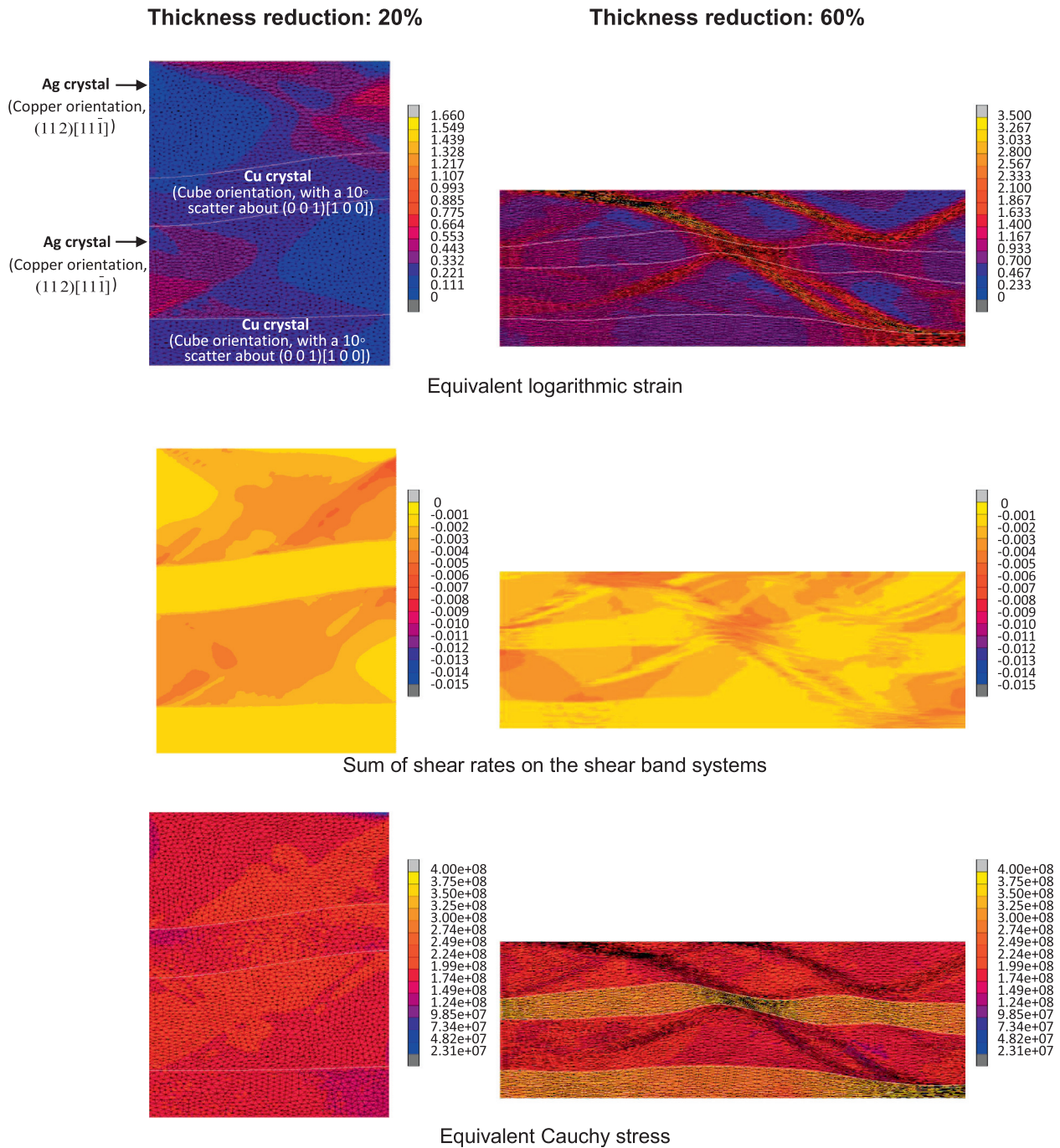

Fig. 6. Predicted distributions of equivalent logarithmic strain, sum of shear rates on the shear band systems and equivalent Cauchy stress for a Cu (Cube orientation, with a 10° spherical Gaussian scattering about $(0\,0\,1)[1\,0\,0]$) plus Ag (Copper orientation, $(1\,1\,2)[1\,1\,1]$) heterophase bicrystal at 20% and 60% thickness reductions. White lines indicate interfaces between the abutting crystals. Finite element mesh is not shown in the second row of results for better visibility of the distribution of shear bands.

the different deformation mechanisms as a function of the equivalent true strain for Cu single crystal with the Cube orientation (with a 10° scatter about the $(001)[100]$orientation) are shown in Fig. 2. It is shown that, unlike the Goss orientation, in which shear banding never occurs during the whole deformation range studied, in the Cube-oriented crystal a shear contribution of 0.1 from shear banding can be identified at ~57% deformation (0.85 true strain). Fig. 6 shows the predicted distribution of equivalent logarithmic strain, the sum of shear rates on the shear band systems and the equivalent Cauchy stress for the deformed Cu (Cube orientation, with a 10° scatter) plus Ag $((112)[11\bar{1}])$ bicrystal. At 20% thickness reduction, the largest strain is located at the left and right bounding edges in the Ag phase, which agrees with the strain distribution of the Copper-oriented Ag single crystal. At those regions with localized strain, significant shear banding is also identified. In the Cu phase, no strain localization or shear banding is observed. Since the shear band systems in the Cube-oriented crystal are activated at a later deformation stage compared with the $(112)[11\bar{1}]$orientation, the simulation results for the Cu–Ag sample up to 60% deformation are presented. As shown in the right column of Fig. 6, at a higher thickness reduction, significant strain localization that penetrates phase boundaries appears. Moreover, shear banding is clearly identified at the strain localized region in the Cu phase. These shear bands corresponding to the occurrence of localized strain induce severe curvature of the phase boundaries. Even though the Cu phase is stronger than the Ag phase, as seen in the distribution of the equivalent Cauchy stress, the elements inside the shear banding region of the hard phase (Cu) have been severely narrowed along the ND. Consistent results are also predicted in other bicrystals (Fig. 3a, b, Fig. 4a and c), which are in general agreement with the experimental observations reported on cold rolled Cu–Ag [25,26] and Cu–Nb [27] composites. As revealed by the bicrystal simulations, the curved lamellar structure is a result of local plastic instability in the shear banding region, and, as rolling reduction increases, the shear propagates further along the shear band direction. Therefore, at large deformations a single shear band can propagate through several crystals in the multilayered microstructure. This observation can explain the cross-interface deformation found in heterophase MMC. According to recent atom probe results obtained on heavily deformed Cu–Ag and Cu–Ag–Nb composites [22,25], substantial alloying occurs in shear bands where large numbers of lattice dislocations penetrate through the heterophase-interfaces among the constituent phases. Then, when shear banding becomes the dominant deformation mechanism in either phase of the composites, chemical mixing on an atomic scale among the abutting phases can be facilitated by shear transfer in shear bands across the phase boundaries [50].

In fact, shear band development in the Cu–Ag and Cu–Nb heterophase MMC under plane strain deformation is a clear example of the effect of microstructures on co-defor-mation mechanisms. In this work, quantitative influences of microstructures on the micromechanisms are studied by performing a series of simulations of corresponding bicrystal samples with specific orientation and phase combinations. One of the important findings is that shear banding behavior of an individual crystal is affected not only by the inherent properties of the crystal, but also by the presence and behavior of its abutting crystals. More specific, interfaces present in the heterophase composites show a similar effect on shear band formation as a microbanded microstructure that is considered a prerequisite for shear banding [14,15,46]. Therefore, for accurate prediction of shear banding behavior of bulk composite materials, continuum models should be qualified to predict localized stress and strain fields, and thus the occurrence of such collective deformation mechanisms by incorporating realistic microstructure topologies. Atomic-level experimental investigations and simulations for MMC with respect to structures of heterophase interfaces, atom mixing and interface migration [51–53] could guide the development of an advanced mesoscopic constitutive model for such systems. However, this effort is beyond the scope of the current study.

5. Conclusions

CPFE simulations of the shear banding behavior in plane strain compressed Cu–Ag and Cu–Nb MMC using two-dimensional bicrystal models were presented. To reveal the underlying micromechanics and co-deformation of the materials, characteristic initial heterophase microstructures of the MMC were considered. The main results are as follows.

1. Significant non-crystallographic shear banding occurs in the fcc and bcc crystals, depending on the specific initial orientations.
2. To accommodate deformation between adjacent phases in the bicrystal samples, pronounced shear bands are triggered by stress concentrations at the interfaces (phase boundaries). This leads to highly localized strains within the bands. The shear band development in an individual crystal is strongly related to the initial orientation of the crystal and also to the mechanical properties and orientations of its abutting crystals.
3. The predicted topology and nature of the cross-phase shear bands, i.e. the extreme local strains, significant bending of the heterophase interface regions and sharp strain localization that propagates across the interfaces, agree well with experimental observations made on cold-rolled composites. The simulations reveal that cross-phase shear banding leads to highly localized values of stress and strain at interfaces. These features, although not explored here, are essential for understanding the micromechanical boundary conditions inside co-deformed composites and the associated shear-induced chemical mixing.

Acknowledgements

Appendix A. Supplementary material

Supplementary data associated with this article can be found, in the online version, at http://dx.doi.org/10.1016/j.actamat.2013.04.029.

References

[1] Duggan BJ, Hatherly M, Hutchinson WB, Wakefield PT. Metal Sci 1978;12:343.
[2] Haratani T, Hutchinson WB, Dillamore IL, Bate P. Metal Sci 1984;18:57.
[3] Hirsch J, Lücke K. Acta Metall 1988;36:2863.
[4] Ushioda K, Hutchinson WB. ISIJ Int 1989;29:862.
[5] Donadille C, Valle R, Dervin P, Penelle R. Acta Metall 1989;37:1547.
[6] Tvergaard V, Needleman A. Proc Roy Soc Lond A 1993;443:547.
[7] Batra RC, Zhu ZG. Acta Mech 1995;113:185.
[8] Paul H, Driver JH, Maurice C, Jasieński Z. Mater Sci Eng A 2003;359:178.
[9] Nguyen-Minh T, Sidor JJ, Petrov RH, Kestens LAI. Scripta Mater 2012;67:935.
[10] Paul H, Morawiec A, Driver JH, Bouzy E. Int J Plast 2009;25:1588.
[11] Duckham A, Knutsen RD, Engler O. Acta Mater 2001;49:2739.
[12] Paul H, Morawiec A, Bouzy E, Fundenberger JJ, Piątkowski A. Metall Mater Trans A 2004;35:3775.
[13] Paul H, Driver J, Maurice C, Piątkowski A. Acta Mater 2007;55:575.
[14] Wagner P, Engler O, Lücke K. Acta Metall Mater 1995;43:3799.
[15] Wagner P, Engler O, Lücke K. Texture Microstruct 1991;14:927.
[16] Hong CS, Tao NR, Huang X, Lu K. Acta Mater 2010;58:3103.
[17] Xiao GH, Tao NR, Lu K. Scripta Mater 2008;59:975.
[18] Bevk J, Harbison JP, Bell JL. J Appl Phys 1978;49:6031.
[19] Verhoeven JD, Chumbley LS, Laabs FC, Spitzig WA. Acta Metall Mater 1991;39:2825.
[20] Embury JD, Han K. Curr Opin Solid State Mater Sci 1998;3:304.
[21] Sauvage X, Thilly L, Lecouturier F, Guillet A, Hono K, Blavette D. Phase transformation in nanostructured materials produced under heavy plastic deformation. Amsterdam: Elsevier Science Bv.; 2000.
[22] Sauvage X, Renaud L, Deconihout B, Blavette D, Ping DH, Hono K. Acta Mater 2001;49:389.
[23] Quadir MZ, Ferry M, Al-Buhamad O, Munroe PR. Acta Mater 2009;57:29.
[24] Li YP, Tan J, Zhang GP. Scripta Mater 2008;59:1226.
[25] Ohsaki S, Kato S, Tsuji N, Ohkubo T, Hono K. Acta Mater 2007;55:2885.
[26] Davy CA, Han K, Kalu PN, Bole ST. IEEE Trans Appl Supercond 2008;18:560.
[27] Raabe D, Heringhaus F, Hangen U, Gottstein G. Z Metallkd 1995;86:405.
[28] Raabe D, Mattissen D. Acta Mater 1998;46:5973.
[29] Raabe D, Ohsaki S, Hono K. Acta Mater 2009;57:5254.
[30] Raabe D, Heringhaus F, Hangen U, Gottstein G. Z Metallkd 1995;86:416.
[31] Jia N, Roters F, Eisenlohr P, Kords C, Raabe D. Acta Mater 2012;60:1099.
[32] Roters F, Eisenlohr P, Hantcherli L, Tjahjanto DD, Bieler TR, Raabe D. Acta Mater 2010;58:1152.
[33] Anand L, Su C. J Mech Phys Solids 2005;53:1362.
[34] Wang YM, Chen MW, Zhou FH, Ma E. Nature 2002;419:912.
[35] Kuhlmann-wilsdorf D, Wilsdorf H. Acta Metall 1953;1:394.
[36] Nemat-Nasser S, Guo W. Mater Sci Eng A 2000;284:202.
[37] Raabe D, Ball J, Gottstein G. Scripta Metall Mater 1992;27:211.
[38] Carpenter JS, Vogel SC, LeDonne JE, Hammon DL, Beyerlein IJ, Mara NA. Acta Mater 2012;60:1576.
[39] Beyerlein IJ, Mara NA, Bhattacharyya D, Alexander DJ, Necker CT. Int J Plast 2011;27:121.
[40] Jia N, Lin Peng R, Wang YD, Johansson S, Liaw PK. Acta Mater 2008;56:782.
[41] Hartig C, Mecking H. Comput Mater Sci 2005;32:370.
[42] Raabe D, Roters F. Int J Plast 2004;20:339.
[43] Jia N, Eisenlohr P, Roters F, Raabe D, Zhao X. Acta Mater 2012;60:3415.
[44] Hölscher M, Raabe D, Lücke K. Acta Metall 1994;42:879.
[45] Kuroda M, Tvergaard V. Int J Plast 2007;23:244.
[46] Korbel A, Martin P. Acta Metall 1986;34:1905.
[47] Kalidindi SR, Bronkhorst CA, Anand L. J Mech Phys Solids 1992;40:537.
[48] Raabe D, Zhao Z, Roters F. Scripta Mater 2004;50:1085.
[49] Basson F, Driver JH. Acta Mater 2000;48:2101.
[50] Raabe D, Choi P-P, Li YJ, Kostka A, Sauvage X, Lecouturier F, et al. MRS Bull 2010;35:982.
[51] Mishin Y, Asta M, Li J. Acta Mater 2010;58:1117.
[52] Han WZ, Carpenter JS, Wang J, Beyerlein IJ, Mara NA. Appl Phys Lett 2012;100:011911.
[53] Wang J, Misra A, Hoagland RG, Hirth JP. Acta Mater 2012;60:1503.